AIMS Materials Science
AIMS Materials Science, 12(5): 975–992.
DOI: 10.3934/matersci.2025044
Received: 02 July 2025
Revised: 17 September 2025
Accepted: 22 September 2025
Published: 25 September 2025

https://www.aimspress.com/journal/Materials

Research article

Three-dimensional examination of fly ash-PVCA composite reinforced by expanded polystyrene beads using X-ray micro-tomography

Saleh Eladaoui[1], Mouad El Mouzahim[1,2], El Mehdi Eddarai[1,*], Maroua Maaroufi[3], Mustapha El Kanzaoui[1], Abdelkabir Bellaouchou[1], Abdelkader Zarrouk[1,4] and Ratiba Boussen[1]

[1] Laboratory of Materials, Nanotechnology, and Environment, Faculty of Sciences, Mohammed V University in Rabat, Av. Ibn Battouta, Agdal-Rabat, BP 1014, Morocco
[2] Department of Chemistry, Life Sciences and Environmental Sustainability, University of Parma, INSTM, UdR Parma, Parco Area delle Scienze 17/A, Parma, 43124, Italy
[3] Université Paris-Saclay, CentraleSupélec, ENS Paris-Saclay, CNRS, Laboratoire de Mécanique Paris-Saclay, 91190, Gif-sur-Yvette, France
[4] Research Centre, Manchester Salt & Catalysis, unit C, 88-90 Chorlton Rd, M15 4AN, Manchester, United Kingdom

* **Correspondence:** Email: elmehdi.eddarai@gmail.com.

Abstract: In this study, we performed a multi-scale three-dimensional (3D) analysis of a new type of lightweight composite material made with coal fly ash and expanded polystyrene wastes. For this, a methodology for identifying and quantifying the microstructure property of the lightweight composite material was developed using X-ray micro-tomography. The material studied mainly contained polystyrene beads, which have approximately the same density as the air voids; they share the same grayscale, and it is not easy to distinguish them, which makes it challenging to characterize the porous 3D structure of this material. The 3D visualization software “Avizo” enabled the 3D reconstruction of the composite and its microstructural characterization. Several microstructure parameters were explored and characterized quantitatively, including porosity distribution, pore surface area, representative elementary volume (REV), sphericity, pore equivalent diameter, and pore network model. The results demonstrated that X-ray micro-tomography is a valuable instrument for non-destructive and complete detection of the microstructural properties of polystyrene reinforced composite.

Keywords: lightweight composite material; X-ray micro-tomography; expanded polystyrene (EPS); coal fly ash; representative elementary volume (REV); three-dimensional reconstruction

1. Introduction

The development of sustainable materials that are expected to satisfy some requirements such as strength, lightweight, and durability, has received considerable interest. Lightweight composite materials developed using industrial waste products have a lot of potential to impact many different industries. Expanded polystyrene (EPS) is one of those industrial wastes produced on a scale of 15 million tons per year [1] and represents about 10 wt.% of the total plastic waste produced annually since 2008 [2]. It is mostly used for thermal insulation, packaging, and storing of many products because of its flexible structure, shock-absorbing property, impermeability, and mechanical rigidity; EPS also has a stable form in the presence of many chemicals and does not perform chemical reactions except some kinds of acids, solvents, and aliphatic compounds that dissolve it [3–5]. The use of expanded polystyrene waste as lightweight aggregates not only can provide new solutions in the manufacturing of lightweight composite but is also beneficial in terms of environmental protection [6–8]. Research has indicated that lightweight composite concrete can be prepared by adding expanded polystyrene and certain inorganic materials such as fly ash (FA) as raw industrial aggregates [9,10]. Those researchers have concluded that the density, thermal conductivity, and mechanical properties of lightweight composites display a decreasing trend as EPS content increases, which is related to high porosity and low strength of EPS.

Coal fly ash is an industrial solid by-product of coal combustion. The physical properties, as well as the chemical and mineralogical compositions of fly ashes, depend mostly on the source, the composition, and the process of combustion of the coal used in the thermal power plant [11]. Coal fly ash is a mineral mixture mostly composed of a variety of oxides such as SiO_2, and Al_2O_3, as the two major components and metal oxides which can be alkaline, alkaline earth, and transition metal oxides [12,13]. A recent review presented the physicochemical properties of coal fly ash and its potential applications. The researchers reported that the reuse of fly ash in soil improvement, the construction industry, the ceramics industry, and the synthesis of zeolites remain a good ecological options to minimize the problem of waste disposal and reduce environmental problems, which will add value to the by-products generated by thermal power plants [14].

In recent works, to understand the behavior of expanded polystyrene-based materials at the macroscopic level, it is important to investigate the mechanisms of interaction between the phases of the material at microscopic scale. In this context, several researchers have used X-ray computed micro-tomography to characterize expanded polystyrene reinforced materials at a microscopic scale; Dixit et al. [15] used micro-computed tomography (μCT) to study the microstructural properties of a lightweight-EPS cement composite. The resulting data was used to distinguish polystyrene beads from air voids pores, and therefore to compare the porosity of various mixes; Bouvard et al. [16] investigated the use of fluorescent screen in association with X-ray micro-CT to differentiate polystyrene beads in concrete and then predict the thermal and mechanical properties through various modeling approaches.

In this study, a lightweight composite material made with coal fly ash and expanded polystyrene waste is adopted as the object of research, and a three-dimensional analysis was performed based on

X-ray computed micro-tomography technology to provide the value of porosity and characterize the internal morphology of this composite. An adequate process was used to identify and isolate the phases of the materials and then selecting a representative elementary volume (REV). In addition, several microstructure parameters were explored and characterized quantitatively, including porosity distribution, pore surface area, sphericity, pore equivalent diameter, and pore network model. We aimed for this research to be a reference for understanding the complex and irregular pore structure of polystyrene-based materials and, therefore, for investigating its microstructural characteristics and improving the prediction of their macroscopic behavior. Finally, we not only present the development and microstructural characterization of a new composite material but also contribute to limiting environmental pollution resulting from the disposal of solid and plastic wastes.

2. Materials and methods

2.1. Material and sample preparation

The composite material studied in this work was made by combining two types of wastes: FA and polystyrene beads using wood glue known as polyvinyl acetate (PVCA). The composition of FA-PVCA composite reinforced polystyrene beads is shown in Table 1 in terms of volume ratio. The EPS beads, 4–6 mm in diameter, were spherical in shape and had an extremely very low density around 20 and 30 kg/m^3 [5]. FA was used in this study and obtained from the Supercritical Power Plant of Safi, Morocco, and used without any modifications [17].

Table 1. Composition of FA-PVCA composite reinforced polystyrene.

Materials	Volume ratio
Fly-ash	28%
Polystyrene beads	51%
PVCA	21%

2.2. X-ray micro-tomography

X-ray computed micro-tomography is a non-destructive measurement technique [18], which provides the characterization of the three-dimensional distribution and geometry of pores (i.e., size, sphericity, and volume distribution) in many porous materials without any previous preparation [19], or any changes to their structures [20,21]. This technique has become popular in characterizing the microstructural properties of many materials such as cementitious materials [22,23], metal matrix composites [24,25], and fiber reinforced concrete [26,27]. However, X-ray computed micro-tomography presents major disadvantages related to the limits in spatial resolution and the difficulty to distinguish material components with similar densities.

X-ray computed micro-tomography is based on the absorption of X-rays on material density. When X-rays are performed on the test sample, the intensity of the X-ray beam will be absorbed by the chemical constituents of the material. The transmitted beam creates a series of radiographs called projections for different directions of irradiation. X-ray projections corresponding to various angular positions of the sample are collected using a special detector that transforms X-ray energy into visible radiation (Figure 1). Visible light is transformed into grayscale images, and the resulting images are stacked to reconstruct the three-dimensional structure of material [28]. The gray level obtained on each acquired projection is not only related to the density and absorption capacity of the various components of the material, but also to the energy of the X-rays. Therefore, in radiographic projections, phases with higher-density attenuate more X-rays and appear darker, while low-density phases attenuate fewer X-rays and appear brighter [29,30].

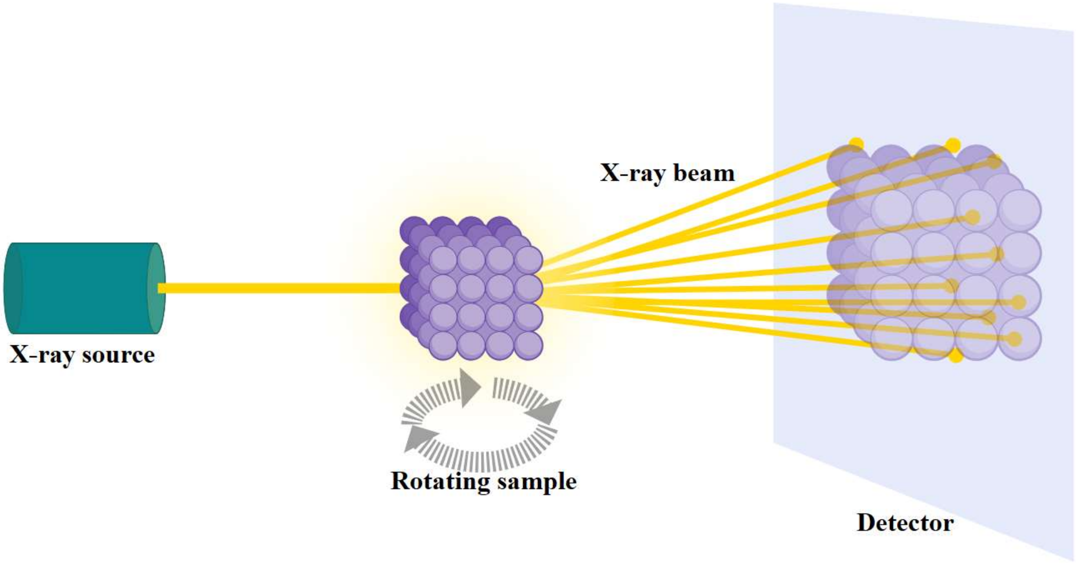

Figure 1. Shematic representation of X-ray tomography principle.

2.3. Image processing

Three large sample sizes (30 × 30 × 30 mm) were scanned at LMPS (Laboratoire de Mécanique Paris-Saclay, France) using the tomograph X50 (North Star Imaging, Rogers, USA), which had a focus tube with focal spot up to 1 μ, a flat-panel detector with a resolution of 256 × 256 pixels, and an adjustable rotary stage. The scans were performed using a microfocus rotating anode X-ray source at controlled conditions of 25 °C and 50% relative humidity. The parameters of the tomograph were the same as those in the study presented by Maaroufi et al. [31], including a tube voltage of 70 kV, a current of 200 μA, and a set of 1200 projections acquired over 360°. The reconstructed volume of the composite was obtained through a filtered back projection algorithm using efX-CT software (efX, North Star Imaging, Rogers, USA) that was compatible with the tomograph X50. Regions of interest were selected from the central part of each reconstructed volume in order to perform the image processing.

The image processing was carried out using Avizo 3D-Image visualization software (Avizo, Thermo Fisher Scientific, Waltham, Massachusetts, USA). It enabled extracting and analyzing pore information inside each zone of interest following a procedure that converted the original raw pixel to a 3D labeled one. The raw volume obtained by the X-ray micro-tomography usually contained some artifacts and noises, which had a negative effect on the quality of the reconstructed volume. A median filter was used to reduce noise and improve the quality of the original raw volume [32].

After the completion of volume filtering, an image segmentation process was followed to detect the porosity apart from the composite matrix and then identify the polystyrene beads and mark them as a distinct phase. To identify the polystyrene beads individually, Avizo software provided an interface composed of four views: a 3D visualization of the sample and three orthogonal slices corresponding to the X, Y, and Z directions. This setup enabled the bead to be located in all three planes and enabled the sample volume to be examined in order to identify each bead one by one. After selecting the bead in the three orthogonal planes, the region of interest was expanded from a manually defined control point. The tolerance parameters of the segmentation tool were adjusted according to local image contrast to prevent the contour from extending beyond the true boundaries of the bead. This approach reduced the risk of misclassification between expanded polystyrene beads and adjacent air voids, thereby improving the reliability of phase boundary determination. This procedure must be repeated for all beads within the sample. They can be easily distinguished from pores by their perfectly spherical shape and their diameter, which ranged between 4 and 6 mm. The main challenge of this method lay in the time and manual effort it required. This process was based on the gray level value of different material phases and also to assume polystyrene beads as a spherical closed macro-pores. The threshold was carefully adjusted on 2D images of XY, XZ, and YZ, and the optimized threshold was applied to the entire slices for 3D volume [33]. Also, the reconstructed volume of the composite was converted to 668 sliced images, and the obtained images were imported to another image processing software, ImageJ (ImageJ, National Institutes of Health, Washington, USA), which enabled us to determine the distribution of the total porosity along the three directions (X, Y, Z). After performing image segmentation, a comprehensive analysis of the 3D volume was conducted to gather detailed information on the characteristics of individual air voids pores and polystyrene beads separately such as volume fraction, sphericity, pore equivalent diameter, and coordination number. The 3D analysis is discussed in detail in the following sections.

3. Results

Figure 2 shows the 3D and 2D Tomographic reconstructed volume with a voxel size of 33 µm of the manufactured composite. We can see that the studied composite material consists generally of two major parts: the light gray pixel is the fly ash-PVCA solid matrix, while the dark gray pixel represents the total porosity, which includes polystyrene beads and air voids. The difference in gray pixel colors was a result of the difference in densities of pores and matrix.

The black phase corresponded to the total porosity (air voids and the polystyrene beads) that is not dense and has a low ability to attenuate X-rays.

The histogram obtained after image processing of the 3D tomographic images using ImageJ software (8-bit format, rescaled from 0 to 250 gray levels) shows two Gaussian distributions equivalent to the two phases (Figure 3). The following results describe the microstructural analysis performed thereafter.

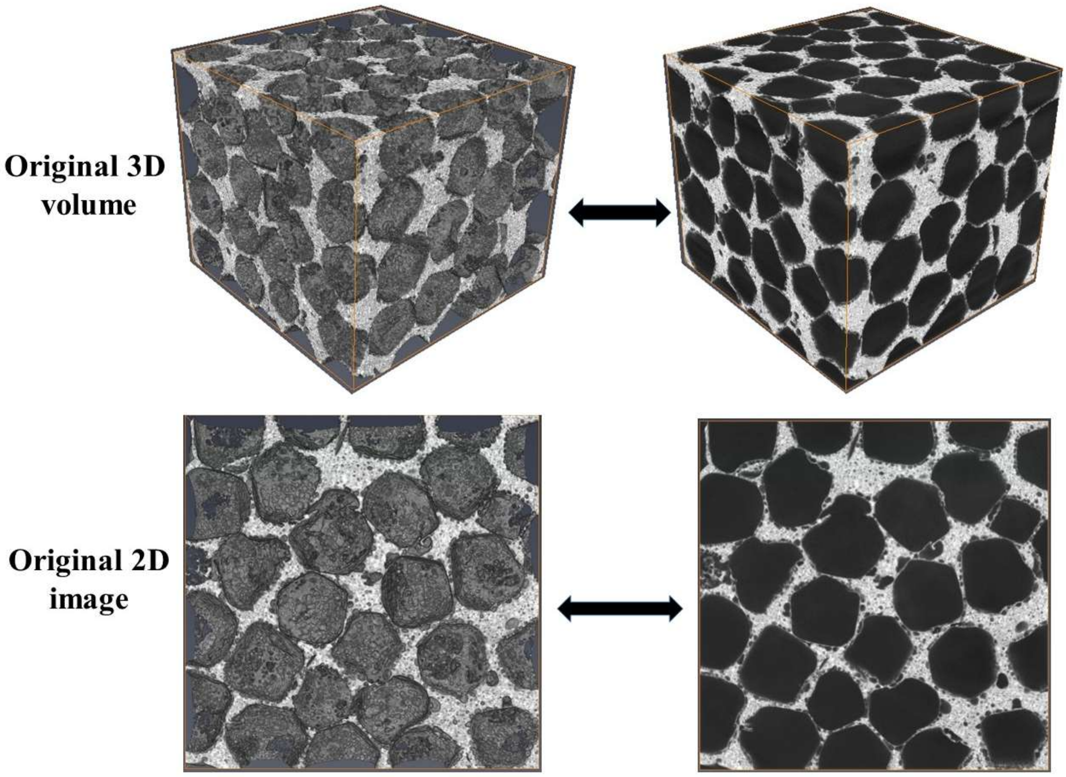

Figure 2. 3D and 2D Tomographic reconstructed volume of the manufactured composite corresponds to 739 × 733 × 793 voxels. Voxel size is 33 μm.

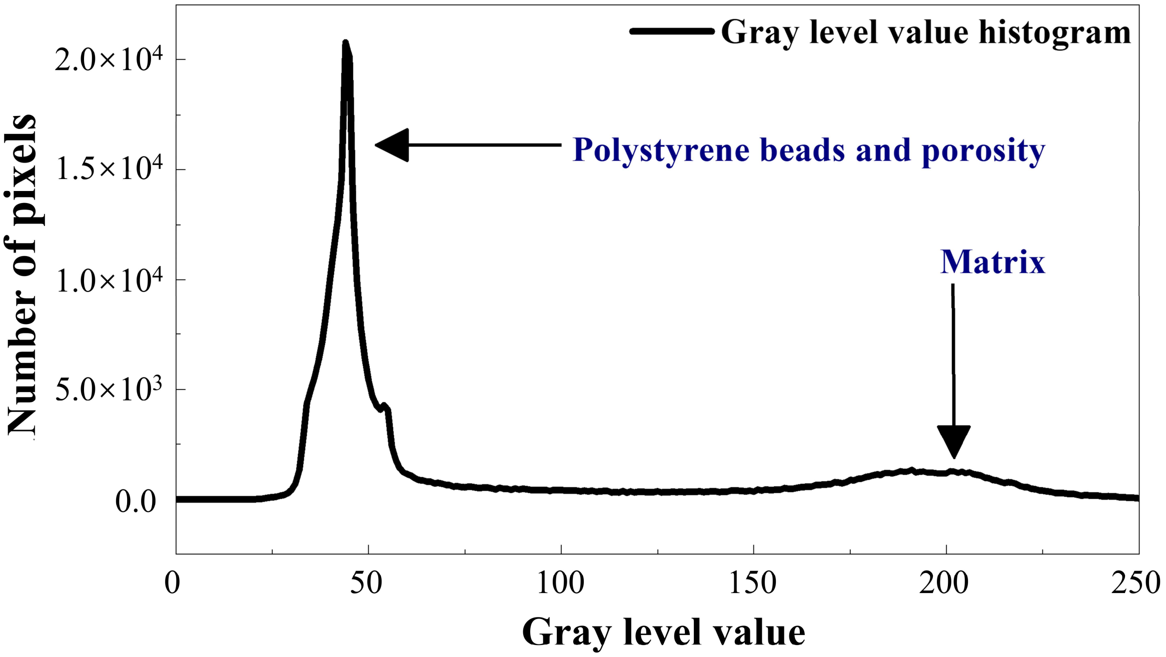

Figure 3. Gray levels histogram of the 3D reconstructed tomographic volume of the composite.

3.1. Two-dimensional characterization

In this part, a two-dimensional reconstruction of the volume of interest was performed. The individual 2D pores in the XY, XZ, and YZ directions of the obtained sliced images were identified and analyzed using the label analysis model in Avizo software, which enabled us to calculate the surface area of each single 2D pore in one sliced image. Figure 4 illustrates the distribution of pore area in the XY, XZ, and YZ directions as a function of pores frequency. It was found that the pore areas were between 10^6 and 4.5×10^7 µm^2 in all three directions, and more than 84% of total pore areas were smaller than 10^7 µm^2; and the other 16% of areas pores were higher than this value.

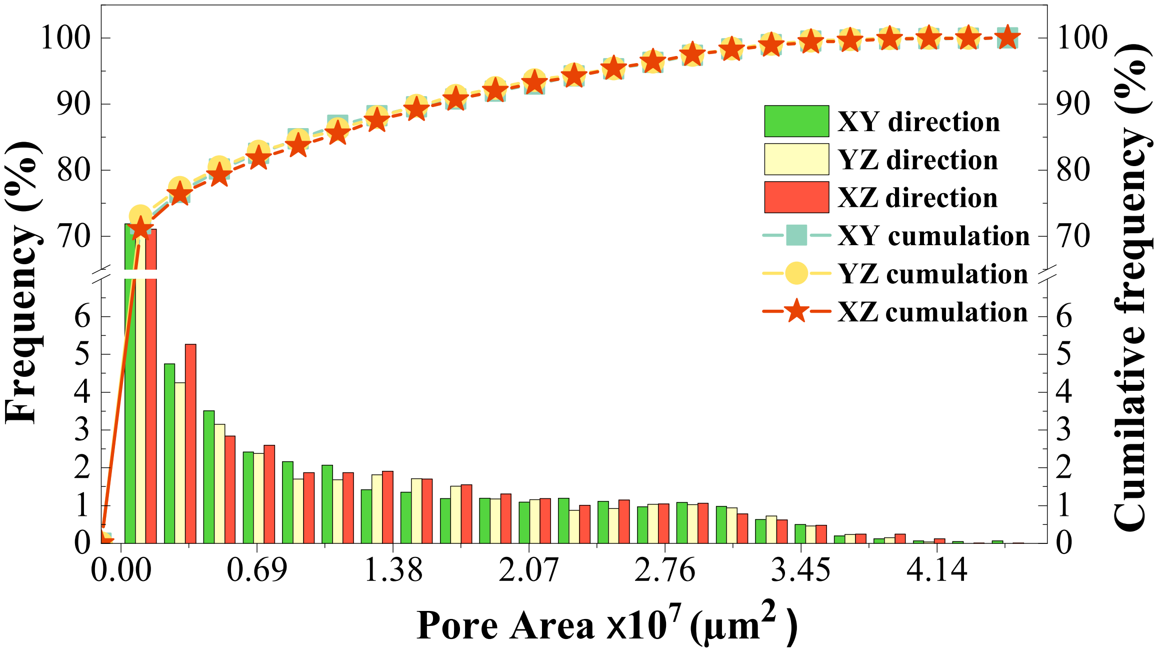

Figure 4. Pore area distribution of total pores (air voids and EPS beads) along the three directions (X, Y, and Z).

This non-uniform distribution of pores in three directions could be confirmed by determining the evolution of total porosity along the X, Y, and Z-directions. The distribution of total porosity (air voids pores and EPS beads) along the three directions X, Y, and Z was determined based on the average porosity in each slice image. The results of the analysis are presented in Figure 5, whereby comparing the three curves, the total porosity shows a significant variation and an arbitrary distribution in all directions. In addition, large fluctuations of porosity values between two successive images can also be observed, which generally indicates many discontinuities; this result proves the inhomogeneity and the non-uniform distribution of pores of the composite material.

Figure 5. Distribution of the total porosity (pores and EPS beads) in the three directions (X, Y, and Z).

3.2. Determination of representative elementary volume

Figure 6 shows the REV determination using successive porosity measurements of EPS reinforced composite in terms of the edge of the selected sub-volume. Therefore, observed that the cubic zone of 11 × 11 × 11 mm^3 was the REV in our work, and the measured porosity was around 7.7%.

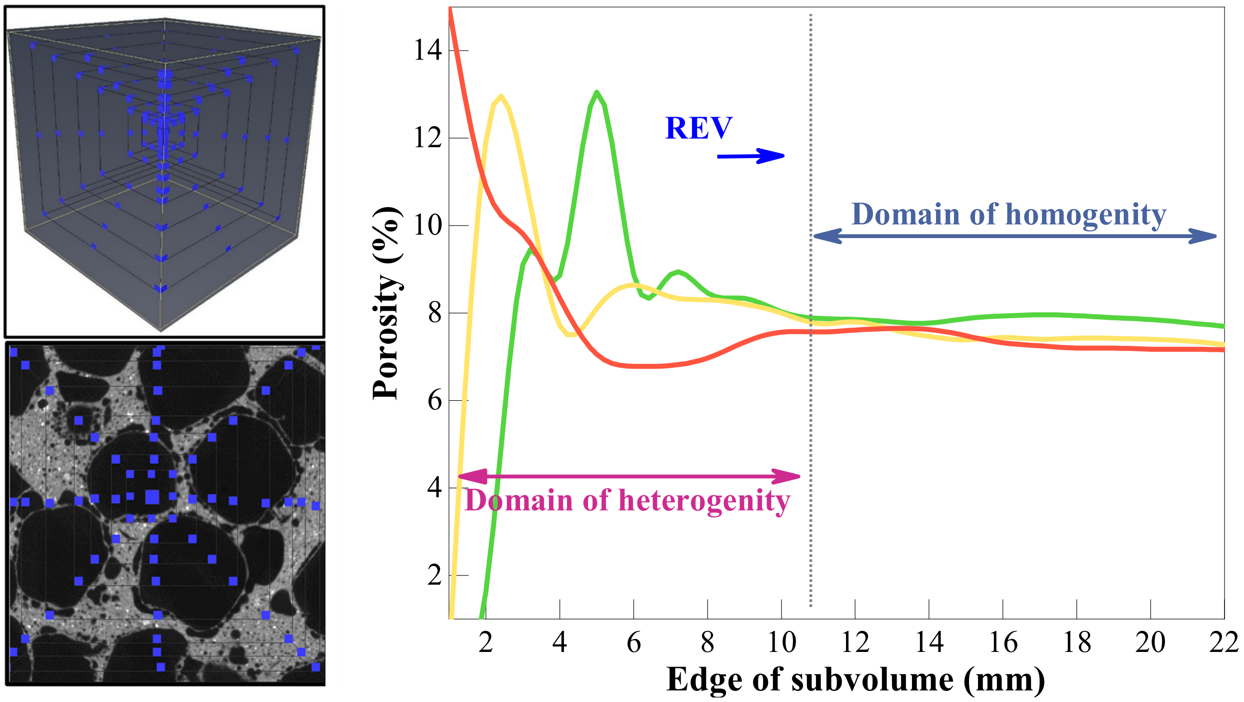

Figure 6. REV based on porosity measurements.

3.3. 3D pore analysis

In order to individualize the pores from the matrix and to analyze the relationship between the number of pores and the volume of pores, a 3D segmentation analysis process was adapted using Avizo software. The distribution of pore volumes as a function of frequency and volume fraction is illustrated in Figure 7, showing that pore frequency decreased while volume fraction increased with pore volume. Also, pores with a volume less than 10^{10} μm^3 constituted 94.5% of all pores, but their volume fraction accounted for only 2.7%; on the contrary, pores with a volume greater than 10^{10} μm^3 constituted only 5.5% of all pores, but their volume fraction covered up around 97% of the total pore volume.

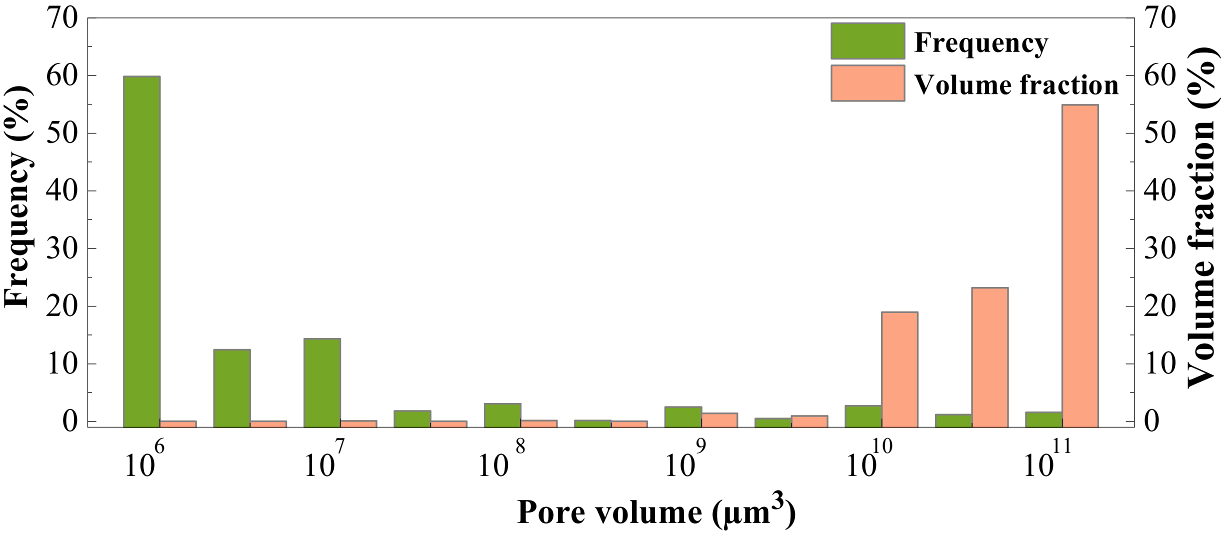

Figure 7. Distribution of the volume of pores.

To better understand this result, a 3D volume rendering of pores was performed using a module in Avizo to separate the pores according to their volume, and therefore illustrated the morphology and structure of the pores at different sizes and shapes in three dimensions, as presented in Figure 8. The figure shows that with increasing pore volume (groups a to f), the regularity of pore geometry became apparent, and the large pores (groups e and f) were spherical.

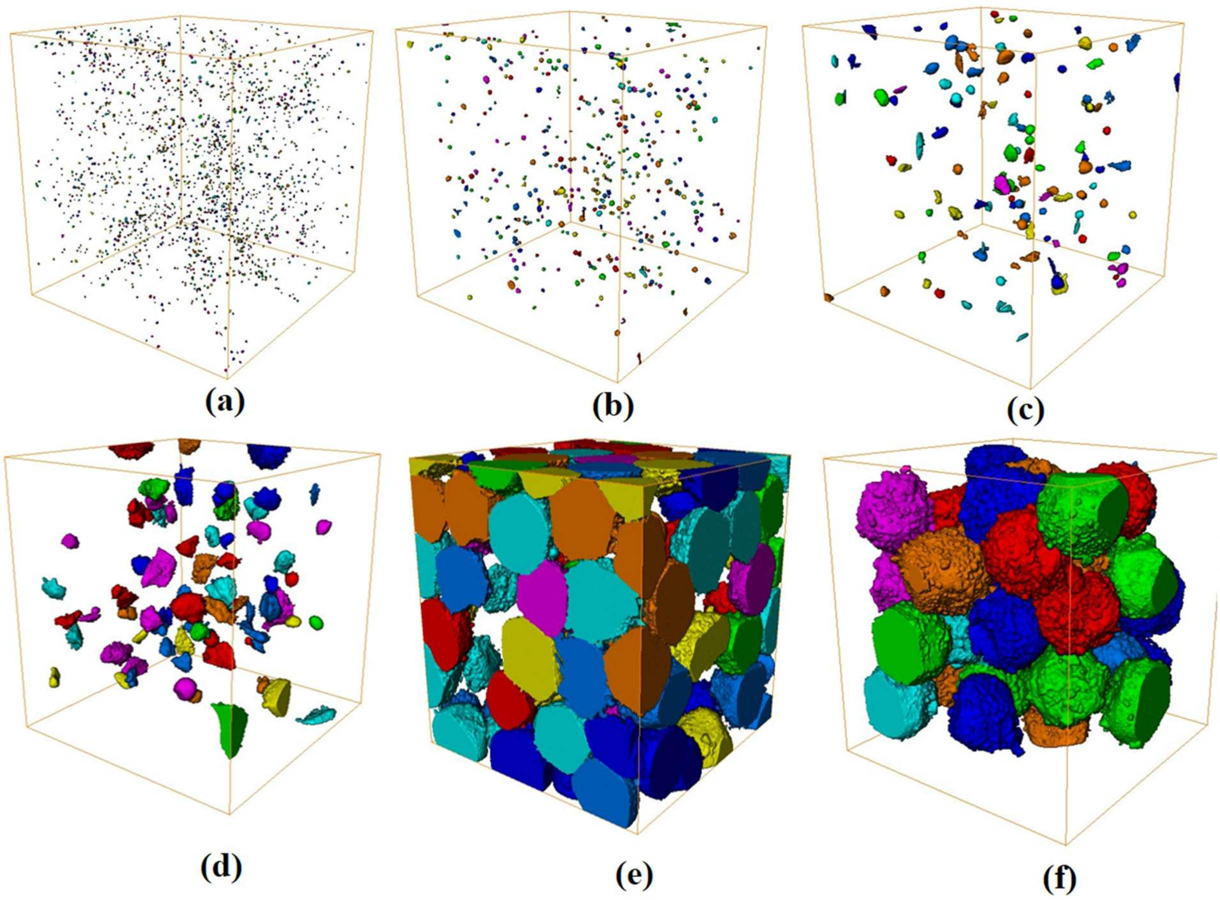

Figure 8. 3D volume rendering of classified pores based on the pore volume range (μm^3): (a) (10^6, 10^7], (b) (10^7, 10^8], (c) (10^8, 10^9], (d) (10^9, 10^{10}], (e) (10^{10}, 10^{11}], and (f) $>10^{11}$.

3.4. Sphericity analysis

In this part, an additional microstructural analysis of pore morphology properties was performed by characterizing the sphericity and 3D pore equivalent diameter. For a given pore, sphericity is a quantitative parameter that characterizes the closeness of the pore shape to a real sphere. For a sphericity value of one, the pore is considered a perfect sphere, and any pore that is not a sphere will have values less than one.

Sphericity is obtained by the following Eq 1:

$$Sphericity = \frac{\pi^{1/3} \times (6V)^{2/3}}{A} \tag{1}$$

where V (μm^3) is the volume of the pore and A (μm^2) is the surface area of the pore [34].

Moreover, the equivalent diameter is the diameter of a sphere having the same volume as a specific pore and is defined as Eq 2:

$$Equidiameter = \sqrt[3]{\frac{6 \times Volume_{3d}}{\pi}} \tag{2}$$

where $Volume_{3d}$ is the 3D volume of a given pore [35].

Figure 9 shows the sphericity distribution of total pores (air voids and polystyrene beads) of the composite. As observed, the values of Sphericity of individualized polystyrene beads were mostly concentrated between 0.5 and 0.8, while the sphericity of air void pores was in the range of 0.4 and 1, and most of these air voids had a sphericity higher than 0.9. We note that the sphericity of some air void pores was greater than 1, which can be explained by the presence of too small pores [36].

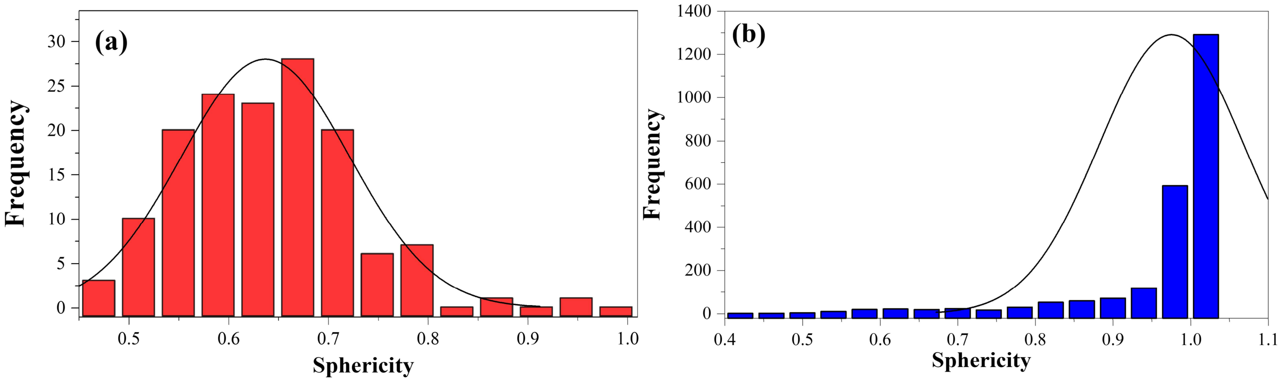

Figure 9. Sphericity distribution of total pores of the composite: (a) sphericity of individualized polystyrene beads, and (b) sphericity of air void pores.

Moreover, to determine whether the difference in pore sphericity distribution was associated with pore size, a diagram of sphericity versus eqdiameter was plotted. It can be seen from the Figure 10 that the plot is in a large area and has no obvious curvilinear relationship.

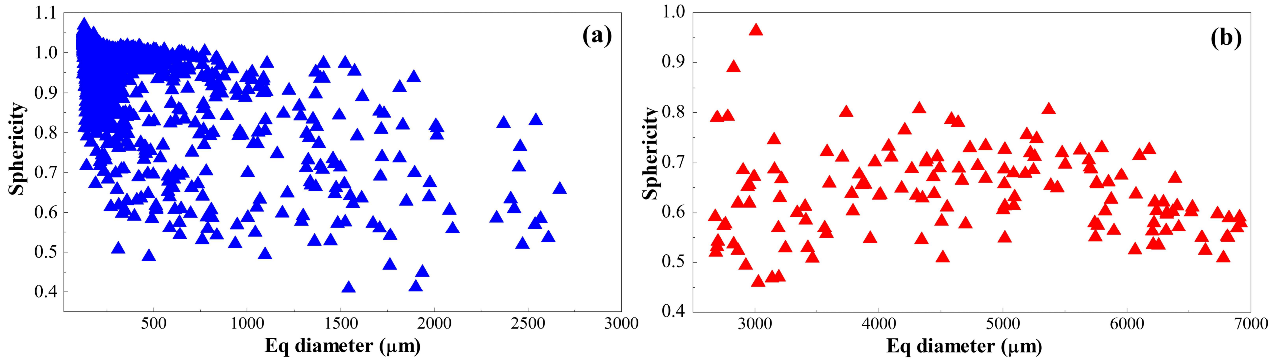

Figure 10. Distribution of sphericity versus equivalent diameter: (a) sphericity of air voids pores, and (b) sphericity of individualized polystyrene beads.

3.5. Pore network model

Our objective of this part was to describe the connection between polystyrene beads based on their structure using the pore network model in Avizo. The process of extracting the pore network model is illustrated in Figure 11 and consists of: (1) creating a binary model by separating the total pores (polystyrene and air voids pores) from the matrix; then (2) individualizing the polystyrene beads using the filter by measure range module in Avizo to separate the pores according to their volume; and (3) generating the corresponding spheres and tubes, which constituted the pore network model [37–39]. Figure 12 shows the coordinate number distribution of individualized EPS beads, where the coordination numbers were distributed between 1 and 12, and the average coordination number of each bead throat was 5.48.

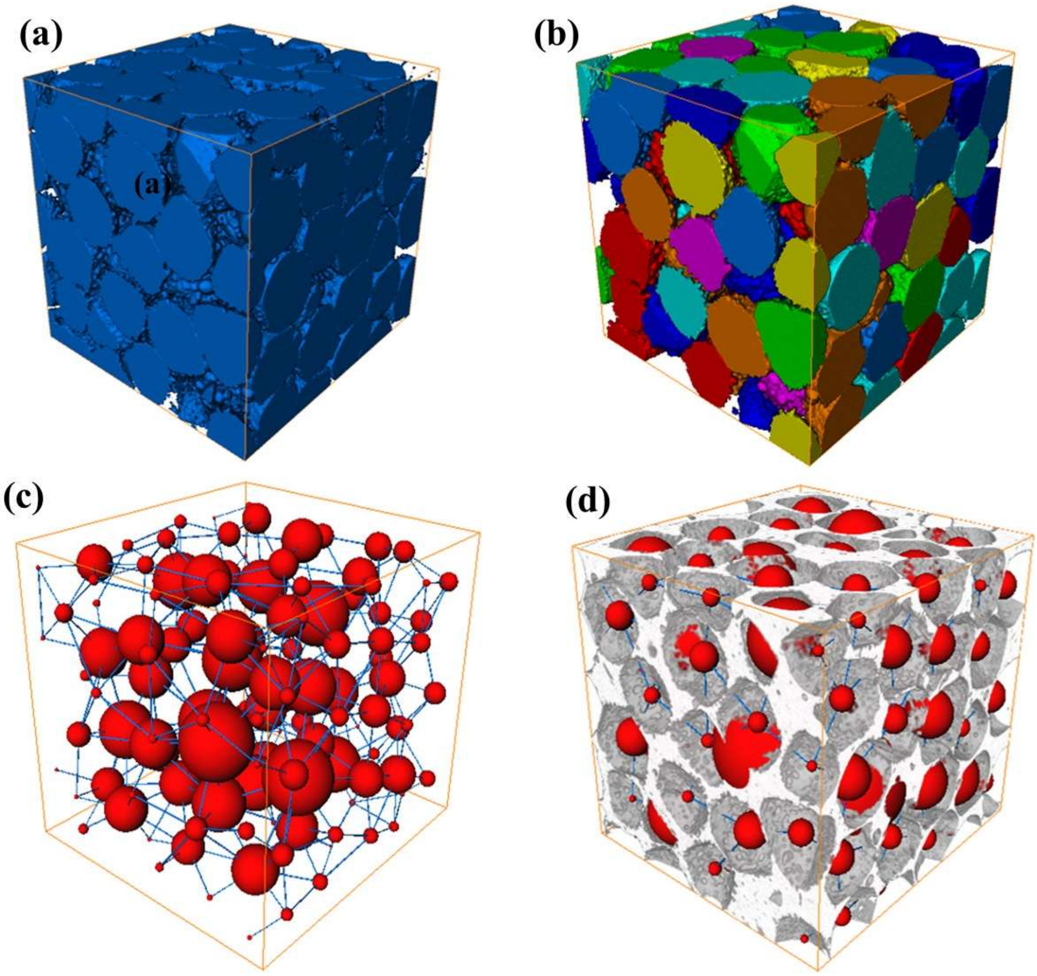

Figure 11. Construction of the pore network model: (a) binary model of total pore (air voids and polystyrene beads); (b) segmentation model of individualized polystyrene beads; (c) pore network model (red spheres correspond to polystyrene beads and blue tubes correspond to throats); and (d) pore network model-material matrix.

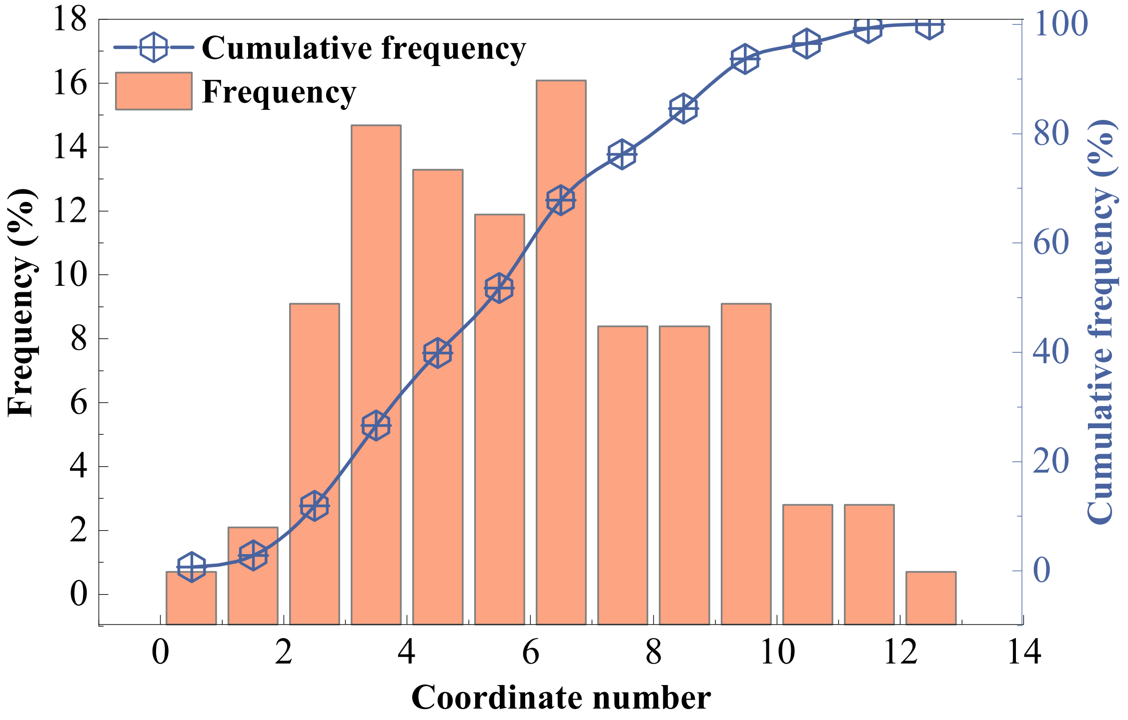

Figure 12. Distribution histogram of individualized EPS coordinate numbers.

4. Discussion

For the 3D and 2D Tomographic reconstructed volume of the manufactured composite (Figure 2), the EPS beads contain 98% air, no more than 2% polystyrene, and have approximately the same density as air voids [40]. Therefore, they share the same grayscale values, and the distinction between them is difficult. However, using Avizo software, a limiting threshold is used to identify and differentiate all the polystyrene beads separately. A gray level histogram, generated by processing the 3D tomographic images with ImageJ software, is used to confirm the existence of two distinct phases in the studied material. In addition, the pore area distribution of total pores equivalent to the two phases (Figure 4) indicates that most 2D pores are small and can be attributed to air void pores; however, large size area pores represent polystyrene beads. The analysis of the pore surface shows that the pores are non-uniformly distributed in three directions. On the other hand, it is reported in the literature that the REV is the smallest volume that can be measured or simulated to represent the macroscopic behavior of a material [41]. The most commonly method used to determine REV is to consider that the REV is the lowest volume for which the porosity of the composite becomes stable and independent of the size of the sample [42]. To determine the REV, 22 cubic sub-volumes are taken from the center of each sample (three samples in total), with increasing size from 1 × 1 × 1 mm^3 to 22 × 22 × 22 mm^3 (Figure 5). Moreover, the results in Figure 6 indicate the presence of two domains for porosity variations. A domain of heterogeneity where porosity varies considerably; and a domain of homogeneity where the porosity values of the sub-volumes are relatively stable and do not vary significantly. In order to individualize the pores from the matrix and to analyze the relationship between the number of pores and their volume, a 3D segmentation analysis process is implemented using Avizo software (Figure 7). As evident, although small pores are more numerous, they account for only a small proportion of total pore volume. The remaining large pores dominate the total pore volume. Therefore, based on the size and the closed structure of polystyrene beads (Figure 8) used in manufacturing this composite, it is concluded that groups (a to d) represent air void pores; however, groups (e and f) represent polystyrene beads. Consequently, the limit size for defining pores due to air voids is set at 10^{10} μm^3. Any pore exceeding this volume is attributed to polystyrene beads. Therefore, all defects identified in the reconstructed volume are treated as air voids/pores to ensure consistent quantification and to accurately reflect their influence on the overall pore network. Generally, for the sphericity analysis (Figures 9 and 10), the shape of the pores is classified into three groups: spherical ($\psi > 0.8$), disc or rod ($0.5 < \psi \leq 0.8$), and blade ($\psi \leq 0.5$) shapes [43]. The results indicate that polystyrene beads have a disc or rod shape. However, for air void pores, the pores with a smaller size have a spherical shape, while the remaining pores have a disc or rod shape. On the other side, the pore network model based on Avizo (Figure 11) indicate that the red spheres represent the polystyrene beads, and the blue tubes, which connect the polystyrene beads, correspond to the throats. The pore coordination number represents the number of throats to which a pore is connected [44]. The coordination numbers of most air void pores have a value of 0, though they are not considered in this section. In addition, the coordinate number distribution of individualized EPS beads (Figure 12) indicates that the spatial topological structure of the polystyrene beads inside the studied composite has good connectivity.

5. Conclusions

In this work, we have used X-ray micro-tomography to investigate the microstructural properties of fly ash-PVCA composite containing expanded polystyrene beads. The analysis leads to the following conclusions: (1) the 3D volume of the composite material was reconstructed, and a follow-up process enabled us to select and identify all the phases of the studied material. We were able to independently observe fly ash-PVCA matrix, polystyrene beads, and porosity due to air voids. The results give a value of porosity around 7.7% and a REV of $11 \times 11 \times 11$ mm^3. (2) The distribution of total porosity (including porosity and EPS beads) in the matrix, determined using aviso and Image-J software, shows complex microstructural heterogeneity of the composite, which is related to the non-uniform pore distribution in the matrix. (3) The 3D pore structure analysis shows that few large pores representing the polystyrene beads dominate the total volume of the studied composite, and their spatial topological structure has good connectivity. (4) The sphericity of air void pores in the composite is mainly related to the pore size. The results show good sphericity of small pores and complex and irregular sphericity of macro-pores. Furthermore, the good sphericity of the individualized polystyrene beads confirms that its structural morphology remains unchanged during composite manufacturing. (5) The combination of X-ray micro-tomography and image processing is a useful method for non-destructive and complete detection of the three-dimensional information of the fly ash-PVCA composite reinforced by expanded polystyrene beads.

Use of AI tools declaration

The authors declare they have not used Artificial Intelligence (AI) tools in the creation of this article.

Acknowledgments

The first author wishes to acknowledge the Moroccan National Centre for Scientific Research (CNRST) for a scholarship grant.

Author contributions

S. Eladaoui: conceptualization, methodology, investigation, data curation, formal analysis, writing-original draft; M. El Mouzahim: methodology, investigation, formal analysis, writing-original draft; E.M. Eddarai: methodology, investigation, formal analysis, writing-original draft; M. Maaroufi: investigation, data curation, formal analysis, writing-review & editing; M. El Kanzaoui: investigation, formal analysis, writing-review & editing; R. Boussen: investigation, methodology, project administration, resources, supervision, validation, visualization, writing-original draft, writing-review & editing; A. Bellaouchou: supervision, writing-review & editing; A. Zarrouk: supervision, writing-review & editing.

Conflict of interest

The authors declare no conflict of interest.

References

1. Kumar V, Khan A, Rabnawaz M (2022) Efficient depolymerization of polystyrene with table salt and oxidized copper. *ACS Sustain Chem Eng* 10: 6493–6502. https://doi.org/10.1021/acssuschemeng.1c08400
2. Aljabri NM, Lai Z, Hadjichristidis N, et al. (2017) Renewable aromatics from the degradation of polystyrene under mild conditions. *J Saudi Chem Soc* 21: 983–989. https://doi.org/10.1016/J.JSCS.2017.05.005
3. Koksal F, Mutluay E, Gencel O (2020) Characteristics of isolation mortars produced with expanded vermiculite and waste expanded polystyrene. *Constr Build Mater* 236: 117789. https://doi.org/10.1016/j.conbuildmat.2019.117789
4. Ferrándiz-Mas V, Bond T, García-Alcocel E, et al. (2014) Lightweight mortars containing expanded polystyrene and paper sludge ash. *Constr Build Mater* 61: 285–292. https://doi.org/10.1016/j.conbuildmat.2014.03.028
5. Fernando PLN, Jayasinghe MTR, Jayasinghe C (2017) Structural feasibility of expanded polystyrene (EPS) based lightweight concrete sandwich wall panels. *Constr Build Mater* 139: 45–51. https://doi.org/10.1016/j.conbuildmat.2017.02.027
6. Shi G, Liu T, Li G, et al. (2021) A novel thermal insulation composite fabricated with industrial solid wastes and expanded polystyrene beads by compression method. *J Clean Prod* 279: 123420. https://doi.org/10.1016/j.jclepro.2020.123420
7. Colangelo F, Roviello G, Ricciotti L, et al. (2018) Mechanical and thermal properties of lightweight geopolymer composites. *Cem Concr Compos* 86: 266–272. https://doi.org/10.1016/J.CEMCONCOMP.2017.11.016

8. Mucsi G, Szabó R, Nagy S, et al. (2017) Development of polystyrene-geopolymer composite for thermal insulating material and its properties with special regards to flame resistance. *IOP Conf Ser Mater Sci Eng* 251: 012079. https://doi.org/10.1088/1757-899X/251/1/012079
9. Nawghare SM, Mandal JN (2020) Effectiveness of expanded polystyrene (EPS) beads size on fly ash properties. *Int J Geosynth Ground Eng* 6: 6. https://doi.org/10.1007/s40891-020-0189-3
10. Cadere CA, Barbuta M, Rosca B, et al. (2018) Engineering properties of concrete with polystyrene granules. *Procedia Manuf* 22: 288–293. https://doi.org/10.1016/J.PROMFG.2018.03.044
11. Nagrockienė D, Rutkauskas A (2019) The effect of fly ash additive on the resistance of concrete to alkali silica reaction. *Constr Build Mater* 201: 599–609. https://doi.org/10.1016/j.conbuildmat.2018.12.225
12. Bhatt A, Priyadarshini S, Acharath Mohanakrishnan A, et al. (2019) Physical, chemical, and geotechnical properties of coal fly ash: A global review. *Case Stud Constr Mater* 11: e00263. https://doi.org/10.1016/J.CSCM.2019.E00263
13. Wang N, Sun X, Zhao Q, et al. (2020) Leachability and adverse effects of coal fly ash: A review. *J Hazard Mater* 396: 122725. https://doi.org/10.1016/J.JHAZMAT.2020.122725
14. Yao ZT, Ji XS, Sarker PK, et al (2015) A comprehensive review on the applications of coal fly ash. *Earth-Science Rev* 141: 105–121. https://doi.org/10.1016/j.earscirev.2014.11.016
15. Dixit A, Pang SD, Kang SH, et al. (2019) Lightweight structural cement composites with expanded polystyrene (EPS) for enhanced thermal insulation. *Cem Concr Compos* 102: 185–197. https://doi.org/10.1016/j.cemconcomp.2019.04.023
16. Bouvard D, Chaix JM, Dendievel R, et al. (2007) Characterization and simulation of microstructure and properties of EPS lightweight concrete. *Cem Concr Res* 37: 1666–1673. https://doi.org/10.1016/j.cemconres.2007.08.028
17. Kanzaoui M El, Ennawaoui C, Eladaoui S, et al. (2021) Study of the physical behavior of a new composite material based on fly ash from the combustion of coal in an ultra-supercritical thermal power plant. *J Compos Sci* 5: 151. https://doi.org/https://doi.org/10.3390/jcs5060151
18. Bossa N, Chaurand P, Vicente J, et al. (2015) Micro- and nano-X-ray computed-tomography: A step forward in the characterization of the pore network of a leached cement paste. *Cem Concr Res* 67: 138–147. https://doi.org/10.1016/j.cemconres.2014.08.007
19. Olawuyi BJ, Boshoff WP (2017) Influence of SAP content and curing age on air void distribution of high performance concrete using 3D volume analysis. *Constr Build Mater* 135: 580–589. https://doi.org/10.1016/j.conbuildmat.2016.12.128
20. Guo Y, Chen X, Chen B, et al. (2021) Analysis of foamed concrete pore structure of railway roadbed based on X-ray computed tomography. *Constr Build Mater* 273: 121773. https://doi.org/10.1016/j.conbuildmat.2020.121773
21. Qsymah A, Sharma R, Yang Z, et al. (2017) Micro X-ray computed tomography image-based two-scale homogenisation of ultra high performance fibre reinforced concrete. *Constr Build Mater* 130: 230–240. https://doi.org/10.1016/j.conbuildmat.2016.09.020
22. Deboodt T, Ideker JH, Isgor OB, et al. (2017) Quantification of synthesized hydration products using synchrotron microtomography and spectral analysis. *Constr Build Mater* 157: 476–488. https://doi.org/10.1016/j.conbuildmat.2017.09.031
23. Pei Y, Agostini F, Skoczylas F (2017) Rehydration on heat-treated cementitious materials up to 700 °C-coupled transport properties characterization. *Constr Build Mater* 144: 650–662. https://doi.org/10.1016/j.conbuildmat.2017.03.100

24. Yuan R, Singh SS, Liao X, et al. (2020) Fracture analysis of particulate metal matrix composite using X-ray tomography and extended finite element method (XFEM). *J Compos Sci* 4: 62. https://doi.org/10.3390/jcs4020062
25. Fan G, Geng L, Wu H, et al. (2017) Improving the tensile ductility of metal matrix composites by laminated structure: A coupled X-ray tomography and digital image correlation study. *Scr Mater* 135: 63–67. https://doi.org/10.1016/J.SCRIPTAMAT.2017.03.030
26. Ríos JD, Leiva C, Ariza MP, et al. (2019) Analysis of the tensile fracture properties of ultra-high-strength fiber-reinforced concrete with different types of steel fibers by X-ray tomography. *Mater Des* 165: 107582. https://doi.org/10.1016/J.MATDES.2019.107582
27. Ríos JD, Cifuentes H, Leiva C, et al. (2019) Analysis of the mechanical and fracture behavior of heated ultra-high-performance fiber-reinforced concrete by X-ray computed tomography. *Cem Concr Res* 119: 77–88. https://doi.org/10.1016/J.CEMCONRES.2019.02.015
28. Korat L, Ducman V, Legat A, et al. (2013) Characterisation of the pore-forming process in lightweight aggregate based on silica sludge by means of X-ray micro-tomography (micro-CT) and mercury intrusion porosimetry (MIP). *Ceram Int* 39: 6997–7005. https://doi.org/10.1016/j.ceramint.2013.02.037
29. Chen B, Lin W, Liu X, et al. (2019) Pore structure development during hydration of tricalcium silicate by X-ray nano-imaging in three dimensions. *Constr Build Mater* 200: 318–323. https://doi.org/10.1016/j.conbuildmat.2018.12.120
30. Meftah R, Berger S, Jacqus G, et al. (2019) Multiscale characterization of glass wools using X-ray micro-CT. *Mater Charact* 156: 109852. https://doi.org/10.1016/j.matchar.2019.109852
31. Maaroufi M, Abahri K, El hachem C, et al. (2018) Characterization of EPS lightweight concrete microstructure by X-ray tomography with consideration of thermal variations. *Constr Build Mater* 178: 339–348. https://doi.org/10.1016/j.conbuildmat.2018.05.142
32. Moradian M, Hu Q, Aboustait M, et al. (2019) Direct in-situ observation of early age void evolution in sustainable cement paste containing fly ash or limestone. *Compos Part B* 175: 107099. https://doi.org/10.1016/j.compositesb.2019.107099
33. Yin S, Chen X, Yan R, et al. (2021) Pore structure characterization of undisturbed weathered crust elution-deposited rare earth ore based on X-ray micro-CT scanning. *Minerals* 11: 236. https://doi.org/https://doi.org/10.3390/min11030236
34. Sun J, Yan K, Zhu Y, et al. (2021) A high-similarity modeling method for low-porosity porous material and its application in bearing cage self-lubrication simulation. *Materials* 14: 5449. https://doi.org/https://doi.org/10.3390/ma14185449
35. Feng Z, Dong X, Fan Y, et al. (2020) Use of X-ray microtomography to quantitatively characterize the pore structure of three-dimensional filter cakes. *Miner Eng* 152: 106275. https://doi.org/10.1016/j.mineng.2020.106275
36. Jing G, Xu K, Feng H, et al. (2020) The non-uniform spatial dispersion of graphene oxide : A step forward to understand the inconsistent properties of cement composites. *Constr Build Mater* 264: 120729. https://doi.org/10.1016/j.conbuildmat.2020.120729
37. Li Y, Chi Y, Han S, et al. (2021) Pore-throat structure characterization of carbon fiber reinforced resin matrix composites: Employing micro-CT and Avizo technique. *PLoS One* 16: 9. https://doi.org/10.1371/journal.pone.0257640

38. Desbois G, Urai JL, Hemes S, et al. (2016) Multi-scale analysis of porosity in diagenetically altered reservoir sandstone from the Permian Rotliegend (Germany). *J Pet Sci Eng* 140: 128–148. https://doi.org/10.1016/j.petrol.2016.01.019
39. Luo X, Zhang Y, Zhou H, et al. (2022) Pore structure characterization and seepage analysis of ionic rare earth orebodies based on computed tomography images. *Int J Min Sci Technol* 32: 411–421. https://doi.org/10.1016/j.ijmst.2022.02.006
40. Uttaravalli AN, Dinda S, Gidla BR (2020) Scientific and engineering aspects of potential applications of post-consumer (waste) expanded polystyrene: A review. *Process Saf Environ Prot* 137: 140–148. https://doi.org/10.1016/j.psep.2020.02.023
41. Fan M, Chen Y, Wan K (2021) Representative elementary volume analysis of hardened cement paste during hydration using X-ray computed tomography. *Constr Build Mater* 277: 122268. https://doi.org/10.1016/j.conbuildmat.2021.122268
42. Borges JAR, Pires LF, Belmont Pereira A (2012) Computed tomography to estimate the representative elementary area for soil porosity measurements. *Sci World J* 2012: 526380. https://doi.org/10.1100/2012/526380
43. Schmitt M, Halisch M, Müller C, et al. (2016) Classification and quantification of pore shapes in sandstone reservoir rocks with 3-D X-ray micro-computed tomography. *Solid Earth* 7: 285–300. https://doi.org/10.5194/se-7-285-2016
44. Rooney EC, Bailey VL, Patel KF, et al (2022) Soil pore network response to freeze-thaw cycles in permafrost aggregates. *Geoderma* 411: 115674. https://doi.org/10.1016/j.geoderma.2021.115674